Earth and Planetary Science Letters 409 (2015) 175–181

Contents lists available at ScienceDirect

Earth and Planetary Science Letters

www.elsevier.com/locate/epsl

# The Eltanin impact and its tsunami along the coast of South America: Insights for potential deposits

Robert Weiss[a], Patrick Lynett[b], Kai Wünnemann[c]

[a] *Department of Geosciences, Virginia Tech, VA 24061, USA*
[b] *Sonny Astani Department of Civil and Environmental Engineering, University of Southern California, Los Angeles, CA 90089-2531, USA*
[c] *Museum für Naturkunde, Leibniz Institute for Evolution and Biodiversity Science, Invalidenstrasse 43, 10115 Berlin, Germany*

ARTICLE INFO

*Article history:*
Received 21 June 2014
Received in revised form 10 October 2014
Accepted 19 October 2014
Available online xxxx
Editor: J. Lynch-Stieglitz

*Keywords:*
Eltanin impact
tsunamis
tsunami modeling
impact cratering
numerical simulations

ABSTRACT

The Eltanin impact occurred 2.15 million years ago in the Bellinghausen Sea in the southern Pacific. While a crater was not formed, evidence was left behind at the impact site to prove the impact origin. Previous studies suggest that a large tsunami formed, and sedimentary successions along the coast of South America have been attributed to the Eltanin impact tsunami. They are characterized by large clasts, often several meters in diameter. Our state-of-the-art numerical modeling of the impact process and its coupling with non-linear wave simulations allows for quantifying the initial wave characteristic and the propagation of tsunami-like waves over large distances. We find that the tsunami attenuates quickly with $\eta(r) \propto r^{-1.2}$ resulting in maximum wave heights similar to those observed during the 2004 Sumatra and 2011 Tohoku-oki tsunamis. We compute a transport competence of the coastal flow and conclude that for the northernmost alleged tsunami deposits, especially for those in Hornitos, Chile, the transport competence is about two orders of magnitude too small to generate the observed deposits.


## 1. Introduction

The Eltanin impact structure belongs to the group of very few impacts that are proven to have hit the marine environment. The reason for this low number of known marine impact structures is multifold. Wünnemann and Lange (2002) calculated a 50% chance for an impactor to hit the deep sea. For an impactor to leave a trace at the ocean floor, the impactor also must have a certain diameter or larger. The Eltanin impact itself can be taken as a threshold diameter because the impact did not form a crater, but impact-cratering processes and the water flow created by water displacement during the impact process generated indications to link this structure to an impact. However, the unequivocal evidence for the impact origin is given by the finding of remnants of the impactor in drill cores. For much smaller impactors than the Eltanin impactor, water waves would have of course been formed as well. However, it remains to be seen if the water flow alone is violent enough to leave behind specific indications to be recognized as an impact; if the shock wave does not reach the sea floor, none of the classical impact evidence, such as shock metamorphosed rocks or mineral phases, will be generated.

The Eltanin impact occurred about 2.15 million years ago in the Bellinghausen Sea, Antarctica. The black circle in Fig. 1 annotated with "E" marks the location of the Eltanin impact site. The Eltanin impact did not produce a typical bowl-shaped impact crater. It only reworked the sea-bed substrate and produced chaotic layering of the sediment, which was first recognized by Kyte et al. (1981). Gersonde et al. (1997) also found spherules and the well-known Iridium anomaly. The latter two are evidence of the impact, and the fact that a crater was not formed was used by Mader (1998), Wünnemann and Lange (2002) and Shuvalov and Trubetskaya (2007) to constrain an impactor diameter. These three independent modeling efforts estimated the Eltanin impactor to be between 0.7 km and 1 km in diameter, assuming a Stony meteorite ($\rho_i \approx$ 2700 kg m$^{-3}$). However, in a more recent study (Shuvalov and Gersonde, 2014) estimated the projectile diameter to be between 1.5 and 2 km for a vertical and a 45° impact angle, respectively.

On a large scale, the study published by Ward and Asphaug (2002) is the only publication that considers the propagation and coastal effects of the tsunami generated by the Eltanin impact. The theoretical means that the authors employ to calculate the wave spreading forces the waves to attenuate proportionally to $1/r$, where $r$ is the radial distance from the impact location. Classical shallow-water wave theory, utilized for describing the propagation of earthquake-generated tsunami waves, only includes geometrical spreading, which means that the amplitude of the propagating

*E-mail address:* weiszr@vt.edu (R. Weiss).

http://dx.doi.org/10.1016/j.epsl.2014.10.050
0012-821X/

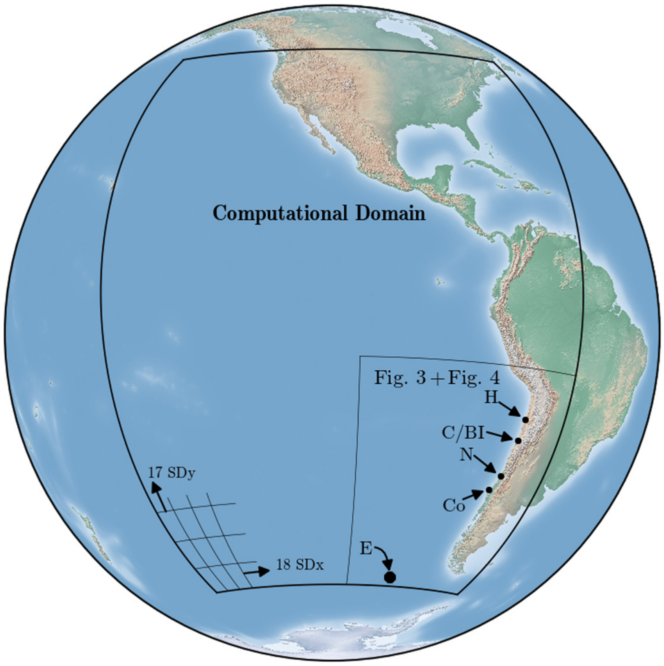


**Fig. 1.** The rectangle projected on the sphere represents the computational domain. The location of the Eltanin impact size is marked with E. The sites of potential tsunami deposits formed by the Eltanin impact tsunami are: H – Hornitos, C/BI – Caldera and Bahia Inglesa, N – Navidad, and CO – Concepcion. $SD_x$ and $SD_y$ refer to the computational subdomains used for the wave modeling. There are 18 longitudinal and 17 latitudinal subdomains resulting 306 subdomains in our state-of-the-art, high-performance numerical simulations of the wave dynamics.

**Table 1**
Wave amplitude $\eta$ proportional to $1/\sqrt{r}$, $1/r$ and $1/r^2$ for 10 km, 50 km, 100 km, and 200 km distance from the impact center and an initial amplitude of $\eta(r=0) = 100$ m.

| | | Distance | | | |
|---|---|---|---|---|---|
| | | 10 (km) | 50 (km) | 100 (km) | 200 (km) |
| $\eta \propto$ | $1/\sqrt{r}$ | 31.6200 m | 14.1400 m | 10.0000 m | 7.0700 m |
| | $1/r$ | 10.0000 m | 2.0000 m | 0.5000 m | 0.5000 m |
| | $1/r^2$ | 1.0000 m | 0.0400 m | 0.0100 m | 0.0025 m |

wave decreases due to the larger area that the wave engulfs. This leads to an attenuation of the individual waves proportional to $1/\sqrt{r}$. Whether or not the difference in wave amplitudes $\eta(\vec{x}, t)$ is $\eta(\vec{x}, t) \propto 1/r$ or $\eta(\vec{x}, t) \propto 1/\sqrt{r}$ is enormous. Table 1 gives an example how wave amplitudes changes proportional to $1/\sqrt{r}$, $1/r$ and $1/r^2$.

Does the Eltanin impact generate a tsunami that attenuates with $\eta(\vec{x}, t) \propto 1/r$ or other $q$'s in $\eta(\vec{x}, t) \propto r^{-q}$. Given the example for $1/r$ and $1/\sqrt{r}$ the consequences for the projected wave amplitudes arriving at shorelines around the Pacific, especially for the south American continent, are significant. In this regard, Ward and Asphaug (2002) state that maximum wave amplitudes along the coastline of the South American continent decrease from about 200 m in the south to about 30 to 40 m in the north.

These significant maximum wave amplitudes and their associated flows may have created tsunami deposits along the South American continent. The South American continent is uplifting due to the subduction process. The uplift process makes sedimentary deposits available that were at sea-level about 2 Ma ago. Hartley et al. (2001) and others suggested that a few unusual sedimentary deposits, such as the deposits at Hornitos (H in Fig. 1; i.e., Hartley et al., 2001) are ascribed to Eltanin impact. The aim of our study is to explore whether the wave amplitudes that arrive along the South American continent are sufficient to move the grain sizes of these proposed tsunami deposits. Our analysis is based on impact modeling with iSALE (Wünnemann et al., 2006), wave modeling with different wave theories (Lynett and Liu, 2002), and simple estimates of critical shear stresses to see which grain sizes could be transported.

## 2. Eltanin tsunami deposits along the Chilean coast

The development of western South America has long been governed by subduction and plate tectonics. The subduction and associated processes created a very complicated geologic situation which is recorded in sediments in the coastal area. However, these processes work on different time and length scales at different parts of the subduction zone, which results in poorly constrained correlations of sediments in different areas along the western coast of South America. The discussion about deposits that might belong to the Eltanin impact tsunami is an excellent example of this uncertainty. There are five prominent locations at which the Eltanin impact tsunami allegedly left evidence of its presence behind. However, this evidence is often circumstantial and tainted by poor stratigraphic constraints. Going from north to south, Hornitos is located at the Mijeones Peninsula (H in Fig. 1). The tsunami origin of the seven to ten-meter thick conglomerate bed was first put forward by Hartley et al. (2001) and reiterated by Goff et al. (2012). This bed contains large (approximately 5 m in diameter) angular to very angular boulders that are situated in a matrix of poorly sorted fine to very coarse sandstone. The basal part of this conglomerate has an erosional contact with the underlying strata. The second deposit is at Caldera and Bahia Inglesa (C/BI in Fig. 1). The deposits at Caldera consist of a debris-flow deposit with megaclasts. Also associated with this deposit are well-preserved whale skeletons, which is seen as evidence of long-standing water after the tsunami inundation of the Eltanin impact tsunami (Goff et al., 2012). The potential tsunami deposits at Bahia Inglesa consists of a 42-m thick silt and fine-grained sand stone. Associated with the deposits is a bonebed that contains boulders up to 6 m in diameter. The deposit in Navidad consists of clast-supported conglomerate with angular to subrounded clasts. The fossil assemblage within this deposit indicates a mix of marine and terrestrial origin. This basal conglomerate is overlain by interbedded sand and mudstones as well as conglomerates. The southernmost potential tsunami deposits can be found near Concepcion, where a coarse beach sandstone contains rip-up clasts made up of mudstone. Rip-up clasts are often found in tsunami deposits, such as the deposits left behind by the 1998 tsunami in Papua New Guinea (Gelfenbaum and Jaffe, 2003). This potential tsunami deposit also contains melted quartz and glass particles, which was taken as potential evidence of the Eltanin impact by Goff et al. (2012).

## 3. Theoretical background

### 3.1. Impact modeling

To model the impact process and the generation of waves we use the iSALE-2D shock physics code (Wünnemann et al., 2006), which is based on the SALE hydrocode solution algorithm (Amsden et al., 1980). To simulate hypervelocity impact processes in solid materials, SALE was modified to include an elasto-plastic constitutive model, fragmentation models, various equations of state (EoS), and multiple materials (Melosh et al., 1992; Ivanov et al., 1997). More recent improvements include a modified strength model (Collins et al., 2004) and a porosity compaction model (Wünnemann et al., 2006; Collins et al., 2011) iSALE can simulate fluid flow at all speeds (supersonic and subsonic) and is, therefore, well-applicable to model the generation of large waves resulting from the formation of a crater in the water column. For the simulations presented here, we used the so-called Analytic Equation of State (ANEOS) to calculate the extreme thermodynamic states at high pressure and temperature for water, projectile, and the ocean bottom (Thompson and Lauson, 1972). iSALE has been validated against experiments and benchmarked with other hydrocodes (Pierazzo et al., 2007). Furthermore, iSALE has been used in a number of modeling studies of impact crater formation (Goldin et al., 2006; Kenkmann et al., 2009), in particular, for oceanic impact events and wave generation (Wünnemann and Lange, 2002; Weiss and Wünnemann, 2007). As the most likely scenario for the Eltanin impact event we assume an 750-m diameter stony meteorite (basalt aneos, $\rho = 2700\ \mathrm{kg\,m^{-3}}$) that strikes the surface at $12\ \mathrm{km\,s^{-3}}$ (Mader, 1998; Wünnemann and Lange, 2002; Shuvalov and Trubetskaya, 2007). Note, the impact velocity corresponds to the vertical component of an 18-$\mathrm{km\,s^{-1}}$ oblique impact at 45°, an often used simplification in 2D simulations. The target is composed of a 5000-m deep ocean and a 250-m thick sediment layer (calcite ANEOS) with underlying oceanic crust (basalt ANEOS). The high-resolution computational domain for the impact simulations reaches 50 km radially with a grid spacing of 25 m. The projectile is resolved by 15 cells per projectile radius and the water column resolved by 200 cells. The impact simulations are carried out on a cylindrically symmetric grid that accounts for the effects of geometrical spreading.

### 3.2. Wave modeling

For simulating the dynamics of the generated waves, the pCOULWAVE model (parallel COrnell University Long WAVE, Sitanggang and Lynett, 2005) is used here. pCOULWAVE solves an extended version of the Boussinesq equations. The fluid is assumed to be inviscid, and pCOULWAVE incorporates a moving shoreline with an extrapolation technique (Lynett et al., 2002). Propagation of waves with a wavelength-to-depth ratio of two and greater can be simulated with high accuracy (Nwogu, 1993). The extended-Boussinesq equations of pCOULWAVE are numerically solved with a 4th-order scheme in space and time. Centered finite differences are used for the spatial derivatives and the Adams–Bashforth–Moulton predictor–corrector scheme for the time integration. The numerical solution provides the horizontal velocity vector field and water surface elevation, $\eta$.

The generation of waves takes place with the internal source wavemaker from Wei et al. (1999), modified to recreate the radial impact waves predicted by iSALE in the near field. Sponge layers are placed along lateral boundaries to dissipate wave energy across a wide range of amplitudes and frequencies. The parallelization uses domain decomposition as documented in Sitanggang and Lynett (2005) and paves the way for very large domains, and efficient and robust computations of wave evolution problems, such as published in Park et al. (2013). For the propagation of waves generated by the Eltanin impact, the computational domain reaches from 200° to 300°E and from 50°N to 60°S in Pacific Ocean (Fig. 1). The grid resolution is 2 km, resulting in 306 parallel domains (Fig. 1).

The simulations presented here do not include bottom friction, subgrid dissipation, a breaking model, or any other physical dissipation submodel. Similarly, the numerical scheme uses a fourth-order spatial and temporal integration scheme, and thus numerical dissipation is expected to be minimal. The included physical dispersion prevents the formation of shocks in the open ocean, as might be expected from nonlinear non-dispersive solutions. Therefore, these results might represent, on average, an upper limit of the wave height with respect to dissipation processes; certainly bottom friction would play some role in energy removal over these relatively long lengths of propagation. To test model convergence, grid resolutions from 1 km to 5 km were tested in a smaller, rectangular numerical domain with side length of 300 km, centered at the impact point. It was found that the 3 km resolution provided convergence to within 12% of the radially averaged wave height from the 1 km simulation, and the 2 km resolution was within 3% of the 1 km resolution results. While not computationally feasible to run a 1 km resolution simulation across the entire Pacific Ocean domain, it is reasonable to expect that the 2 km results are sufficient to resolve the primary wave components with wavelengths on the order of 50 km and larger in the open ocean. Furthermore, it is noted that, with wavelengths on this order, in an average ocean depth of 5 km, the dispersive effect represents approximately a 10% correction on the wave and group speeds. Ten's of wavelengths are traveled by these waves before they reach a coastline, and thus, dispersive effects are not negligible.

### 3.3. Coupling of impact and wave model

Aside from the technical and numerical complexities associated with iSALE and pCOULWAVE, also the mathematical form of the differential equations solved in both codes render a full two-way coupling of both codes a very difficult problem. The coupling of both codes here takes advantage of the fact that iSALE can solve all equations in cylindrical coordinates and that the wave maker in pCOULWAVE can be freely forced.

For the connection between iSale and pCOULWAVE, a one-way coupling approach was utilized. A time series of water surface elevation predicted from iSALE at a distance of 17.5 km from the impact center is used to drive a radial wavemaker in pCOULWAVE. Water surface elevation time series output from pCOULWAVE is compared with similar time series maxima from iSALE at distances between 20 and 45 km.

### 3.4. Estimating the transport competence

The largest grain size that is possible to be transported in a specified flow is known as the transport competence. To estimate the transport competence of the flow along the South American continent from the Eltanin impact tsunami, we assume that (a) the flow depth is in the order of the wave amplitude at the 20 m contour, (b) the boundary layer engulfs the entire flow depth, and (c) the Froude number can be used to relate the wave speed with the flow velocity. With the help of the Froude number (assumption c) and the wave amplitude at 20 m (assumption a), we can estimate the flow velocity $\bar{u}_o = Fr\sqrt{g\eta}$. Then we can integrate the law of the wall to compute the critical shear velocity (see also Cheng and Weiss, 2013):

$$u_* = Fr\sqrt{g\eta}\kappa\,\frac{\eta - z_o}{z_o - \eta + \eta * \log(\eta z_o^{-1})} \tag{1}$$

in which $\kappa$ is van Karman's constant ($\approx 0.42$), $\eta$ is the wave amplitude at 20 m water depth, and $z_o$ is Nikuradse's roughness length (a roughness indicator, $\approx d_g/30$). Finally, we can compute the maximum grain size that is possible to move by employing the parameterization of the Shields diagram (Shields, 1936) and axes:

$$X_{cr} = \frac{u_* d_g}{\nu} \tag{2a}$$

$$Y_{cr} = aX_{cr}^b + ce^{dX_{cr}^e} \tag{2b}$$

$$d_g = \frac{\rho u_*^2}{\gamma_s Y_{cr}} \tag{2c}$$

with the coefficients $a = 0.15$, $b = -1.00$, $c = 0.05$, $d = -8.00$ and $e = -0.90$. The parameter $\nu$ is the kinematic viscosity and $\gamma_s$ is

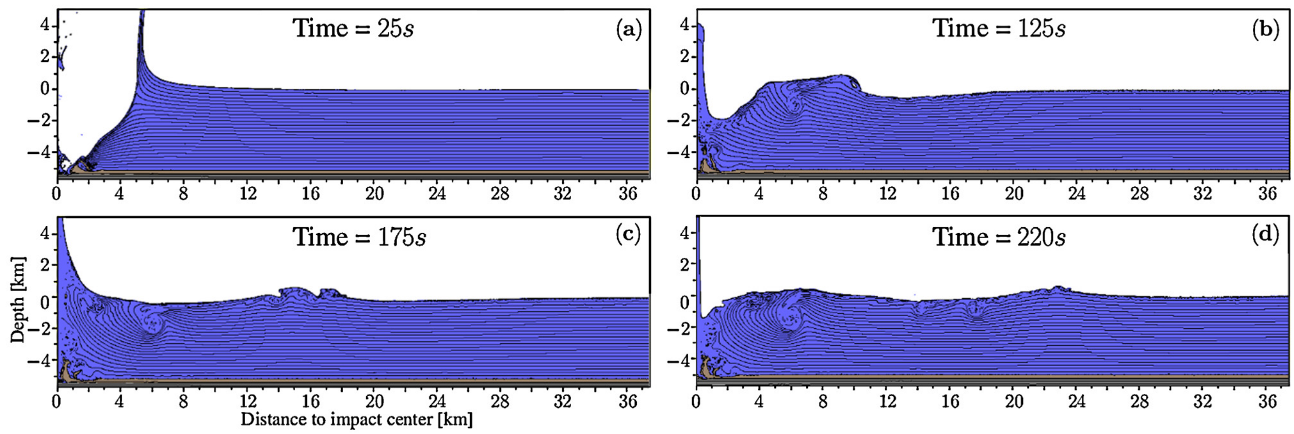


**Fig. 2.** (a)–(d): Different snapshots at four different times showing the generation of large collapse waves in the iSALE simulation of the Eltanin impact.

$\gamma_s = g(\rho_s - \rho)$. Eq. (1) is substituted in Eqs. (2a) and (2c), and then Eqs. (2) are solved iteratively to compute the competence of the flow from the wave amplitude at the 20 m depth contour.

## 4. Results

### 4.1. Impact modeling

Results of the impact modeling with iSALE are shown in Fig. 2 in the form of snapshots at four different times, documenting the generation of tsunamis during the Eltanin impact. Fig. 2(a) shows the displacement of water 25 s after the impactor hits the water surface. The water is displaced in the crater-like geometry. Evidence of the non-linearity of cratering processes can be seen by the fact that the surface portion of the water to which the curtain of ejected water is attached moves away from the center; while the lower portion of the water column moves back toward the center. It should be noted that sediment is entrained in the flow, but a crater is neither formed in the seabed sediments, nor in the underlying oceanic crust.

Eventually the entire water column will accelerate toward the impact center, converge and form a central peak. This central peak of water will collapse and form a wave (Fig. 2(b)). The height of this wave is about one kilometer. Fig. 2(c) shows that while the initial waves are propagating away from the impact site, a second central peak of water is formed whose collapse generates another very large wave (Fig. 2(d)).

The generation of the central peaks repeats itself until the energy for this oscillation is dissipated. As the water piles up to a lower elevation with later central peak formations, the subsequent waves also have smaller wave heights. Furthermore, the generated tsunami is primarily the result of the collapses of these central peaks of water. Wünnemann et al. (2007) referred to these kinds of waves as collapse waves, which are the dominant waves for impacts into deep water (Weiss et al., 2006; Weiss and Wünnemann, 2007).

### 4.2. Wave simulations

The results of the tsunami simulations are shown in Fig. 3(a), which depicts the maximum wave elevation within the computational domain. It should be noted that the color scale is log-normal. It can be seen from this map that the maximum wave elevation quickly decreases from about 200 m to around 10 m with 5° distance from the impact center. Also visible are the “fingers of death”, or areas of refractive focusing, where tsunami energy is concentrated into long and relatively thin bands. These fingers of death are linked to bathymetric features that act as wave guides.

The black line in Fig. 3(b) represents the maximum wave elevation $\max(\eta_c)$ as a function of the distance to the impact site along the line in Fig. 3(a). This graph indicates that $\max(\eta_c)$ decays with a power law due to geometric spreading and other non-linear processes governing the wave evolution. The red line is fitted to the data that has a slope proportional to $1/r^{1.2}$; this spreading exponent represents the best-fit to the pCOULWAVE-modeled height reduction in all directions of propagation away the impact site. For comparison, the two dashed lines represent slopes proportional to $1/\sqrt{r}$, which corresponds to the slope of classical tsunami waves (geometric spreading only), and to $1/r^2$ for highly nonlinear waves. It should be noted that the slope is governed by the wave characteristics that are specific to this particular generation mechanism. The small departure from the linear slope (i.e. exponent equal to one) is ascribed to weak nonlinearity and bathymetric effects.

Fig. 3(b) also shows the maxima of the time series from the iSALE simulations between 20 and 45 km distance from the impact (black circles). The comparison shows the excellent match between iSALE and pCOULWAVE simulations and constitutes that despite the fundamental difference between iSALE and pCOULWAVE, the wave dynamics are simulated adequately.

### 4.3. Transport competence along the coast

With the help of the algorithm outlined in Section 3.4 we can calculate the transport competence of the flow indicated by the maximum wave elevation. The maximum wave elevation can be linked to a maximum flow velocity with the help of the Froude number. The red dots in the center map mark the positions from where the maximum wave elevation are taken for the calculation of the transport competence. Fig. 4 depicts the maximum wave elevation along the coast. From this graph, we can see that the maximum wave elevation along the coast, here denoted with $\max(\eta_c)$, decreases from the south tip of the Southern American continent to the north. Generally south of 45°S, $\max(\eta_c)$ is between six and eight meters. North of this latitude, the maximum wave elevation decreases quickly to values close to zero. The general decrease in $\max(\eta_c)$ can be ascribed to the increasing distance to the impact site. Furthermore, there is also a significant number of spikes present (see Fig. 4). The spikes in the tsunami amplitude reflect the influence of the local bathymetry on amplitude of the approaching tsunami.

With the help of the maximum wave elevation along the coast and the Froude number, the transport competence of the flow can be computed. We understand the transport competence as the largest grain size that the flow can transport. Fig. 4(b) shows the transport competence for a Froude number of $Fr = 1$. Because the transport competence is linked with the maximum wave elevation,

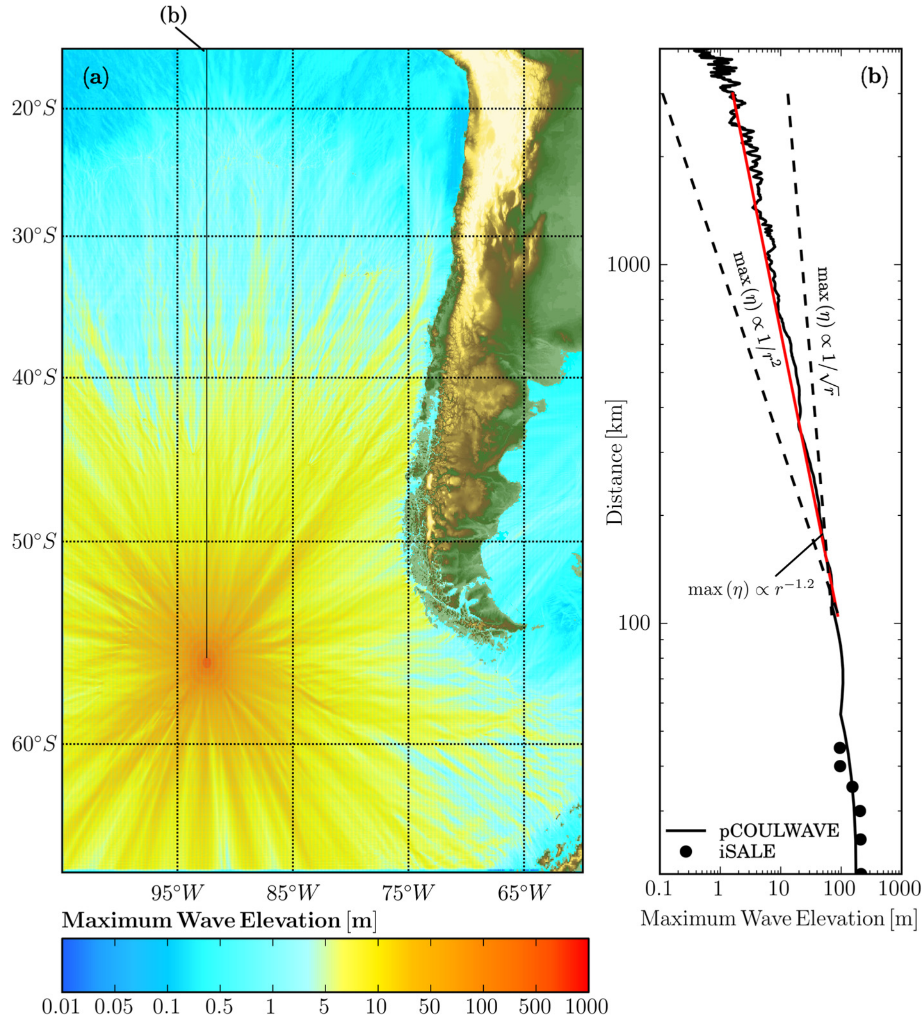


**Fig. 3.** (a) Map of the maximum wave elevation $\max(\eta_c)$ from the Eltanin impact. It should be noted that the color scale is logarithmic. (b) Shows the maximum wave elevation as function of distance to the impact site. The red line has a slope that is proportional to $r^{-1.2}$. The two dashed lines represent the slopes for the classic shallow water wave ($\propto 1/\sqrt{r}$) and a more nonlinear wave ($\propto r^{-2}$). The black circles indicate maxima from iSALE times series.

we can observe a competence of 20 to 30 cm in diameter south of 45°S and only a few centimeters (from 1 to 5 cm in diameter) north of it. The spikes are due to the variations in the maximum wave elevation, and therefore the effect of bathymetry. The scaling factor, by which the given values of the transport competence need to be multiplied, to take different Froude numbers into account, is given in Fig. 4(c).

## 5. Discussion and conclusions

The Eltanin impact generated a tsunami in the South Pacific, and the wave affected the Chilean coast. In our study, we aim to quantify this impact to evaluate whether deposits found along the Chilean coast that might have been formed around the time of the Eltanin impact, could possibly have been formed by the subsequent tsunami.

Our simulation results demonstrate the nonlinear behavior of the waves immediately after generation. Fig. 3 depicts the maximum wave elevation at each point in the computational domain. The maximum wave amplitude near the impact site is about 100 m and decays quickly with increasing difference ($\max(\eta) \propto r^{-1.2}$). The two dashed lines in Fig. 3 give the wave attenuation that is proportional to $1/r^2$ and $1/\sqrt{r}$. Compared with our model results, the wave height driven by $1/\sqrt{r}$ attenuation (individual earthquake-generated tsunami waves) is an order of magnitude larger, and $1/r^2$ is an order of magnitude smaller at a distance of about 1000 km from the impact site.

Along the Chilean coast, the wave amplitude varies from values between 8 and 10 m in the south to less than a meter in the north. While the tsunami-wave amplitude is significant, it is not significantly larger than observed for the earthquake-generated tsunamis in Sumatra 2004 (Titov et al., 2005), 2011 in Japan (Fritz et al., 2012), or even along the central and northern Chilean coast in 2010 (Fritz et al., 2011). We can therefore propose that deep-water impacts as defined in Weiss et al. (2006), Weiss and Wünnemann (2007) have a similar hazard as tsunamis generated by large local earthquakes and only create significantly larger tsunamis near the impact site. If the Eltanin impact had happened in the Atlantic, we can assume that the coastal impact would be even smaller due to the wider shelves of the passive margins in the Atlantic. Nonlinear processes, such as the Van-Dorn Effect (Korycansky and Lynett, 2005) would dissipate even more of the wave energy as the waves travels over the continental slope and shelf regions.

Based on the maximum wave amplitude along the Chilean coast (Fig. 4(a)), we estimate the transport competence of the tsunami flow based on the method described in Section 3.4. For a Froude number of one, the maximum grain-size that can be transported, a.k.a transport competence, is shown in Fig. 4(b) where the red stars represent the maximum grain size found in the four different location of potential Eltanin tsunami deposits. We see that for the

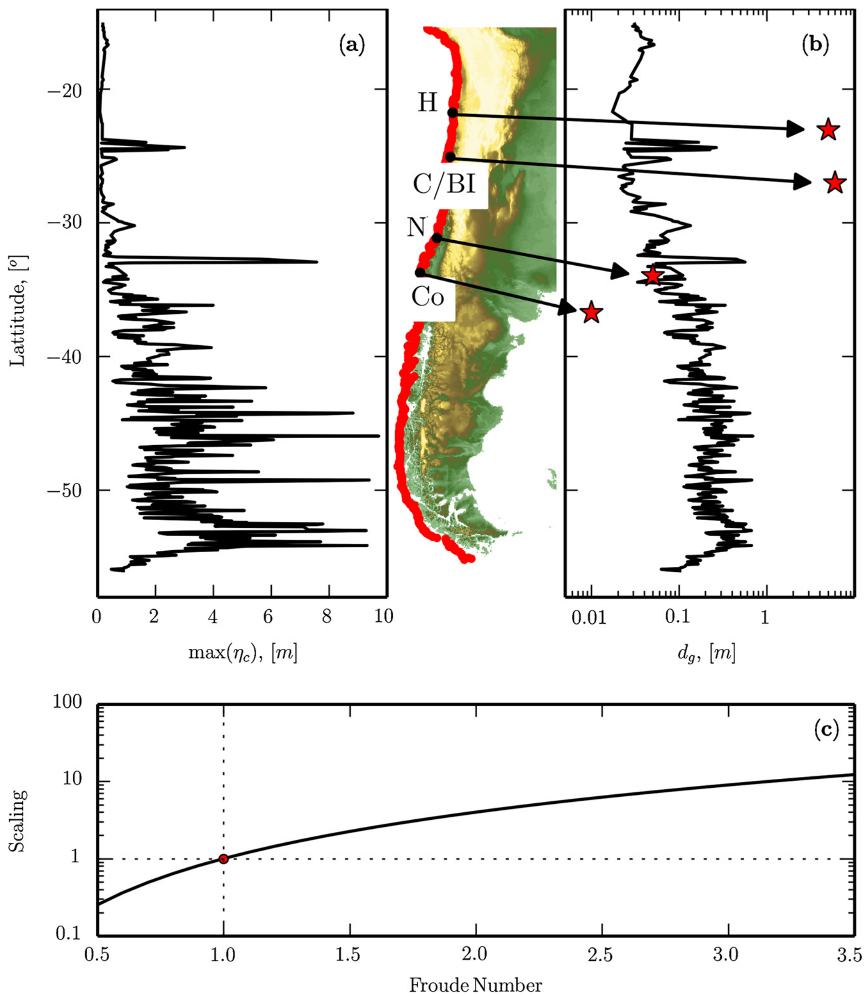


**Fig. 4.** The red dots represent the locations along the coast where the maximum wave elevation is recorded. (a) Maximum wave elevation along the coast. (b) Associated transport competence in meters, and (c) scaling factor as a multiplier for the data in (b) to take different Froude numbers into account.

deposits in Navidad and Concepcion, the simulated flow conditions and the calculated transport competence support the Eltanin origin of the deposits.

However for the deposits in Hornitos, Caldera and Bahia Inlesas, the case is much clearer as the observed grain sizes are much too large to have been transported in the simulated Eltanin tsunami. Even in the case of a Froude number of 3.5, the multiplier of the local values of the transport competence is about 12, which is not enough to shift the transport competence to value larger or equal to the particle diameters from 5 to 6 m found in both places. Again leaving geologic evidence aside, it is physically implausible that the Eltanin tsunami is associated with these deposits. For the deposits in Hornitos, Spiske et al. (2014) and Mather et al. (2014) recently presented compelling evidence indicates that the causative processes are related to landslides in the region.

In general, the basin-wide simulation is a huge computational effort that requires more sophisticated simulation tools than earthquake and perhaps landslide-generated tsunami waves. However, it should be noted that for impacts into deep water, strong wave attenuation will lower the wave amplitude significantly, resulting in shoreline wave elevations that are comparable to recent tsunami observations

## References

Amsden, A., Ruppel, H., Hirt, C., 1980. Sale: a simplified ale computer program for fluid flows at all speeds. Tech. Rep. LA-8095 Report. Los Alamos National Laboratories.

Cheng, W., Weiss, R., 2013. On sediment extent and runup of tsunami waves. Earth Planet. Sci. Lett. 362 (1), 305–309.

Collins, G., Melosh, H., Ivanov, B., 2004. Modeling damage and deformation in impact simulations. Meteorit. Planet. Sci. 39, 217–231.

Collins, G., Melosh, H., Wünnemann, K., 2011. Improvements to the $\epsilon$–$\alpha$ porous compaction model for simulating impacts into high-porosity solar objects. Int. J. Impact Eng. 38 (6), 434–439.

Fritz, H., Petroff, C., Catalan, P., Cienfuegos, R., Winckler, P., Kalligeris, N., Weiss, R., Barrientos, S., Meneses, G., Valderas-Bermejo, C., Almar, R., Dominguez, J., Synolakis, C., 2011. Field survey of the 27 February 2010 Chile Tsunami. Pure Appl. Geophys. 168, 1989–2010.

Fritz, H., Phillips, D., Okayasu, A., Shimozono, T., Liu, H., Mohammed, F., Skanavis, V., Synolakis, C., Takahashi, T., 2012. The 2011 Japan tsunami current velocity measurements from survivor video at Kesennuma Bay using LiDAR. Geophys. Res. Lett. 39, L00G23.

Gelfenbaum, G., Jaffe, B., 2003. Erosion and sedimentation from the 17 July, 1998. Pure Appl. Geophys. 160, 1969–1999.

Gersonde, R., Kyte, F., Bleil, U., Diekmann, B., Flores, J., Gohl, K., Grahl, G., Hagen, R., Kuhn, G., Sierro, F., Völker, D., Abelmann, A., Bostwick, J., 1997. Geological record and reconstruction of the late Pliocene impact of the Eltanin asteriod in the Southern Ocean. Nature 390, 357–363.

Goff, J., Chague-Goff, C., Archer, M., Dominey-Howes, D., Turney, C., 2012. The Eltanin asteroid impact: possible South Pacific paleomegatsunami footprint and potential implications for the Pliocene–Pleistocene transition. J. Quat. Sci. 27, 660–670.

Goldin, T., Wünnemann, K., Melosh, H., Collins, G., 2006. Hydrocode modeling of the Sierra Maera impact structure. Meteorit. Planet. Sci. 21, 1947–1958.

Hartley, A., Howell, J., Mather, A., Chong, G., 2001. A possible Plio-Pleistocene tsunami deposit, Hornitos, northern Chile. Rev. Geol. Chile 28, 117–125.

Ivanov, B., Deniem, D., Neukum, G., 1997. Implementation of dynamic strength models into 2d hydrocodes: applications for atmosphereic breakup and impact cratering. Int. J. Impact Eng. 20, 411–430.

Kenkmann, T., Artemieva, N., Wünnemann, K., Poelchau, M., Elbeshausen, D., 2009. The remarkable meteorite impact event on September 15, 2007, Caracas, Peru: What did we learn? Meteorit. Planet. Sci. 44, 985–1001.
Korycansky, D., Lynett, P., 2005. Offshore breaking of impact tsunami: Van Dorn effect revisited. Geophys. Res. Lett. 32, L10608.
Kyte, F., Zhou, Z., Wasson, J., 1981. High noble metal concentrations in a late pliocene sediment. Nature 292, 417–420.
Lynett, P., Liu, P.L.-F., 2002. A numerical study of submarine landslide generated waves and runup. Proc. R. Soc. Lond. A 458, 2885–2910.
Lynett, P., Wu, T., Liu, P.L.-F., 2002. Modeling wave runup with depth-integrated equations. Coast. Eng. 46 (2), 89–107.
Mader, C., 1998. Modeling the Eltanin asteroid impact. Sci. Tsunami Hazards 16 (1), 17–20.
Mather, A., Hartley, J., Griffiths, J., 2014. The giant coastal landslides of Northern Chile: tectonic and climate interactions on classic convergent plate margin. Earth Planet. Sci. Lett. 388, 249–256.
Melosh, H., Ryan, E., Asphaug, E., 1992. Dynamic fragmentation in impacts: hydrocode simulations of laboratory impact. J. Geophys. Res., 14735–14759.
Nwogu, O., 1993. Alternative form of Boussinesq equations for nearshore wave propagation. J. Waterw. Port Coast. Ocean Eng. 119 (6), 618–638.
Park, H., Cox, D., Lynett, P., Wiebe, D., Shin, S., 2013. Tsunami inundation modeling in constructed environment: a physical and numerical comparison of free-surface elevation, velocity and momentum flux. Coast. Eng. 79, 9–21.
Pierazzo, E., Artemieva, N., Asphaug, E., Cazamias, J., Coker, R., Collins, G.S., Gisler, G., Holsapple, K., Housen, K., Ivanov, B., Johnson, C., Korycansky, D., Melosh, H., Taylor, E., Turtle, E., Wünnemann, K., 2007. The impact hydrocode benchmark and validation project: first benchmark and validation tests. In: Bridging the Gap II: Effect of Target Properties on the Impact Cratering Process.
Shields, A., 1936. Anwendung der Ähnlichkeitsmechanik und der Turbulenzforschung auf die Geschiebebewegung. Mitteilungen der Preussischen Versuchsanstalt für Wasserbau und Schiffbau 26.
Shuvalov, V., Gersonde, R., 2014. Constraints on interpretation of the Eltanin impact from numerical simulations. Meteorit. Planet. Sci. 49 (7), 1171–1185.
Shuvalov, V., Trubetskaya, A., 2007. Numerical modeling of the formation of the Eltanin submarine impact structure. Sol. Syst. Res. 41, 56–64.
Sitanggang, K., Lynett, P., 2005. Parallel computing of a highly nonlinear Boussinesq equation model through domain decomposition. Int. J. Numer. Methods Fluids 49 (1), 57–74.
Spiske, M., Bahlburg, H., Weiss, R., 2014. Pliocene mass failure deposits mistaken as submarine tsunami backwash sediments – An example from Hornitos, northern Chile. Sediment. Geol. 305, 69–82.
Thompson, S., Lauson, H., 1972. Improvements in the chart d radiation-hydrodynamic code 3: revised analytic equation of state. Tech. Rep. SC-RR-71 0714. Sandia Laboratories.
Titov, V., Rabinovich, A.B., Mofjeld, H.O., Thomson, R.E., Gonzalez, F.I., 2005. The global reach of the 26 December 2004 Sumatra tsunami. Science 309 (5743), 2045–2048.
Ward, S., Asphaug, E., 2002. Impact tsunami – Eltanin. Deep-Sea Res. II 49, 1073–1079.
Wei, G., Kirby, J., Sinha, A., 1999. Generation of wave in Boussinesq models using a source function method. Coast. Eng. 36 (4), 271–299.
Weiss, R., Wünnemann, K., 2007. Large waves caused by oceanic impacts of meteorites. In: Tsunami and Non-linear Waves. Springer, Heidelberg, pp. 237–261.
Weiss, R., Wünnemann, K., Bahlburg, H., 2006. Numerical modelling of generation, propagation and run-up of tsunamis caused by oceanic impacts: model strategy and technical solutions. Geophys. J. Int. 167 (1), 77–88.
Wünnemann, K., Lange, M., 2002. Numerical modeling of impact-induced modifications of the deep-sea floor. Deep-Sea Res. II 49, 669–981.
Wünnemann, K., Collins, G., Melosh, H., 2006. A strain-based porosity model for use in hydrocode simulations of impacts and implications for transient crater growth in porous targets. Icarus 180, 514–527.
Wünnemann, K., Weiss, R., Hofmann, K., 2007. Characteristics of oceanic impact-induced large water waves–re-evaluation of the tsunami hazard. Meteorit. Planet. Sci. 42 (11), 1893–1903.